

Evaluating Coherence of Natural Images by Smoothness Membership in Besov Spaces

Jorge E. Pinzón, John F. Pierce, Compton J. Tucker, and Molly E. Brown

Abstract—Smoothness membership in Besov spaces $\mathcal{B}_q^\alpha(I)$ is used to compare the spatial coherence of satellite images. Smoothness is given by a complexity index computed as the rate of decay of the approximation error $\epsilon(M)$ when the image is approximated by its M -largest quantized wavelet coefficient. The technique was applied to a set of nine normalized difference vegetation index (NDVI) time series data as a quantitative quality measure of spatial coherence. The NDVI data set comprises different compositing and atmospheric correction techniques. The estimates of the complexity index give a quantitative measure of the performance of these techniques that agrees well with visual evaluation and with the physics of the image collection process. We demonstrate the maximum value NDVI composites with Rayleigh, ozone, and water vapor correction consistently provide the highest spatial coherence among the compositing and atmospheric correction techniques evaluated. We also show the complexity index is regionally dependent and is higher in dry periods than in wet periods where residual cloud interference is more likely to appear.

Index Terms—Remote sensing, smoothness of image, wavelets.

I. INTRODUCTION

THE QUALITY assessment of the spatial coherence of natural images poses a challenge to both theoretical and practical image processing. To understand spatial coherence for a particular remote sensing image, one needs to identify artifacts caused by sensor viewing geometry, physical interference, (e.g., cloud contamination), and other atmospheric effects. This must also be coupled with knowledge of subtle details about approximation, uncertainties at the pixel level, and denoising of this particular image type.

NDVI images from the National Oceanic and Atmospheric Administration's (NOAA) advanced very high resolution radiometer (AVHRR) face a number of formidable challenges. They are computed as the normalized difference of the red (ρ_1) and near infra-red (ρ_2) wavelengths: $\text{NDVI} = (\rho_2 - \rho_1)/(\rho_2 + \rho_1)$. Since its inception for monitoring vegetation [1]–[3], the effects of cloud contamination, atmospheric scattering, and absorption on the visible and near-infrared radiances are recognized sources of errors and

uncertainties [4], [5]. Temporal compositing techniques such as maximum NDVI were introduced to increase the opportunity for cloud-free observations and to reduce atmospheric contamination effects [4]. For short compositing periods, where compositing techniques are of limited benefit, atmospheric corrections for Rayleigh, ozone, and water vapor effects are frequently carried out [5]–[7]. However, the spatial coherence of data in this form is degraded by the built-in noise from the varying satellite sensing geometry and from residual clouds or variable atmospheric properties, such as tropospheric aerosols that remain in the data. These built-in noise effects are the most challenging factors to correct due to their spatial and temporal variability.

Woodcock *et al.* [8], [9] and Jupp *et al.* [10] used variograms as a means to understand the nature and causes of spatial variation in images. Their results revealed anisotropy in ground scenes. However, their characterization was limited by the difficulty in interpreting the two-dimensional (2-D) variograms, especially without an appropriate model of ground scenes. They encouraged further research in order to recover better characterization of spatial variability. In another related attempt, Cihlar *et al.* [11] evaluated alternative compositing methods for producing NDVI. Their goal was to obtain a composite image that best approximates a single-date image with a constant near-nadir geometry. The evaluation of the performance of each method was made by visual examination of uniformity. Since a composite image is a mosaic of pixel values that come from different dates and viewing geometries, the evaluation of the spatial coherence cannot be treated properly using this ad hoc rule. To characterize image smoothness, one needs to quantitatively measure errors and uncertainties, a problem that demands a firm mathematical study [12].

The previously noted approaches implicitly assume a spatially Gaussian smooth behavior. For example, the estimation of images with white noise is optimized by finding a representation that discriminates the image from the noise. In this case, Shannon's theory tells us that one should first transform the image into the Karhunen–Loève (K–L) domain, which best encodes a Gaussian process since the resulting coordinates are independent (actually orthogonal) random variables. This assumption is powerfully and implicitly used in geostatistics approaches, e.g., kriging. In fact, the different variogram models used in kriging are derived from Gaussian variogram estimations [8]. However, empirical studies of wavelet transforms of natural images have uncovered markedly non-Gaussian structures [13], [14]. For these more complex (non-Gaussian) images, the Gaussian approximation of the K–L transform is no longer optimal. In fact, a unique optimal K–L will depend on

Manuscript received October 5, 2000; revised May 4, 2001.

J. E. Pinzón is with the Science Systems and Applications, Inc. (SSAI), NASA Goddard Space Flight Center (GSFC), Greenbelt, MD 20771 USA (e-mail: pinzon@negev.gsfc.nasa.gov).

J. F. Pierce is with the Mathematics Department, United States Naval Academy, Annapolis, MD 21402 USA.

C. J. Tucker is with Biospheric Sciences, NASA Goddard Space Flight Center (GSFC), Greenbelt, MD 20771 USA.

M. E. Brown is with the Department of Geography, University of Maryland, College Park, MD 20742 USA.

Publisher Item Identifier S 0196-2892(01)08124-4.

the particular non-Gaussian spatial structure (or geometry) of the image [15].

We instead quantify the spatial coherence of an image by finding its smoothness membership in Besov spaces. This approach is based on the new mathematical framework and applications of harmonic analysis developed by DeVore *et al.* [16], which resulted in a significant impact on recent efforts in denoising [17], [18], compression [16], [19], and registration [20] of natural images. This theory precisely relates the smoothness membership in Besov spaces, the so-called complexity index α , with the rate of decay of the approximation error $\epsilon(M)$ when the image is approximated by its M largest quantized wavelet coefficients. In ordinary language, we introduce the features of the theorems that are pertinent to the spatial coherence issues and set out formally the theorems from DeVore *et al.* [16].

We attempt two goals: 1) to gather the properties of Besov spaces needed for the description of the complexity index in the general setting of wavelet-based methods. Toward this purpose, we shall validate and illustrate the effectiveness of the complexity index describing the spatial coherence in a controllable set of images, i.e., a magnetic resonance image (MRI) at different selected SNRs and 2) to use the complexity index as a quantitative measure of spatial coherence and evaluate the performance of different image compositing and atmospheric correction techniques currently used to create long-term NDVI-AVHRR time series.

II. METHODOLOGY

A. Data

We applied to AVHRR data three different atmospheric correction methods combined with three different 15-day composite procedures and generated nine different NDVI time series. This data set comprised images obtained from the Global Inventory Mapping and Monitoring Study (GIMMS) processing system [21], [23]. There are several AVHRR global land data sets that have been produced [21]–[24]. In the GIMMS data processing chain, the user specifies the map projection, compositing periods, and methods, atmospheric correction, and calibration particulars, and the automated processing system generates the desired rectangular binary file. We have used the Vermote *et al.* [25] 6S scheme to correct Rayleigh, ozone, and water vapor effects. Table I presents the sensitivity of NOAA-AVHRR visible and near infrared channels (channels 1 and 2, respectively) and on the NDVI to atmospheric effects for two different surface land cover types, i.e., bare soil and deciduous forest. The three atmospheric correction methods are: no correction (A0), Rayleigh and ozone correction (A1), and Rayleigh, ozone, and water vapor correction (A3). Three compositing procedures were combined with the atmospheric correction methods. Atmospheric corrections were done on each daily image before the compositing technique was applied [21], [23]. The set of compositing algorithms is as follows.

- Maximum NDVI compositing (VI): this compositing technique is the standard with AVHRR land data because it preferentially selects cloud-free and clear pixels [4]. Its main disadvantage is the angular bias toward the

TABLE I
ATMOSPHERIC EFFECT ON AVHRR DATA COMPUTED BY THE 6S RADIATIVE TRANSFER SCHEME, WHERE r_1 AND r_2 ARE REFLECTANCES OF THE COVER TYPE IN CHANNELS 1 AND 2, RESPECTIVELY. RELATIVE CHANGES ARE GIVEN IN PERCENT [25]

	Ozone 0.247–0.48 (cm/atm)	Water vapor 0.5–4.1 (g/cm ²)	Rayleigh 1013 mb
Channel 1	4.2% to 12% ↘	0.7% to 4.4% ↘	0.02 to 0.06 ↗
Channel 2	—	7.7% to 25% ↘	0.006 to 0.02 ↗
NDVI (bare soil, $r_1 = 0.19$, $r_2 = 0.22$)	0.02 to 0.06 ↗	0.011 to 0.12 ↘	0.036 to 0.094 ↘
NDVI (Deciduous forest, $r_1 = 0.03$, $r_2 = 0.36$)	0.006 to 0.017 ↗	0.036 to 0.038 ↘	0.086 to 0.23 ↘

forward scattering direction that is introduced in selecting observations [11].

- Minimum channel 1 compositing (M1): this technique is very sensitive to cloud shadows, which weaken its applicability to land applications [7].
- Maximum thermal channel 5 compositing (T5): this technique seems to substantially reduce cloud shadows and the likelihood of choosing off-nadir pixels [11]. However, at the extremes of the growing season (over Canada), this method performs poorly due to the similar temperature between cloudy and cloud-free areas [11]. Cihlar *et al.* [11] suggested testing the performance of this method on other geographic areas, in particular, tropical forests.

We processed one year of data by continent in bimonthly composites. The result will be a time series of 24 sample images per method. We have processed continental Africa in 1989 by each of the nine methods and compute not only a global complexity index but also 12 representative regional complexity indexes for each of the 24×9 images in our data set. Regional complexity indexes are computed in order to address the issue of spatial coherence sensitivity to phenologic and climatic variability of land cover type throughout the year. Fig. 1 shows all 13 selected regions, one global and 12 subregions at different resolutions and locations, in which complexity indexes were derived. All regions are square shaped and power of two for application of a fast wavelet transform. Region 2 is the large square region (512×512) that covers most of the center of the continent, thereby completely enclosing regions 3, 9, and 11, and partially enclosing regions 8, 9, and 4. Regions 3, 4, and 5 follow in size (256×256). Region 4 completely encloses region 10 and partially region 11. Table II details relevant seasonal and phenologic characteristics of the 12 subregions. In particular, regions 8, 3, 9, and 11 represent a gradual transition from the (July–September) “summer” rainfall region of the Sahel through the savanna and woodlands, to the equatorial forest with year-round rains [26]–[29].

B. Wavelets

In this section, we describe the generic multiresolution method for computing wavelet decompositions. Although multiresolution wavelet decomposition is at the core of the

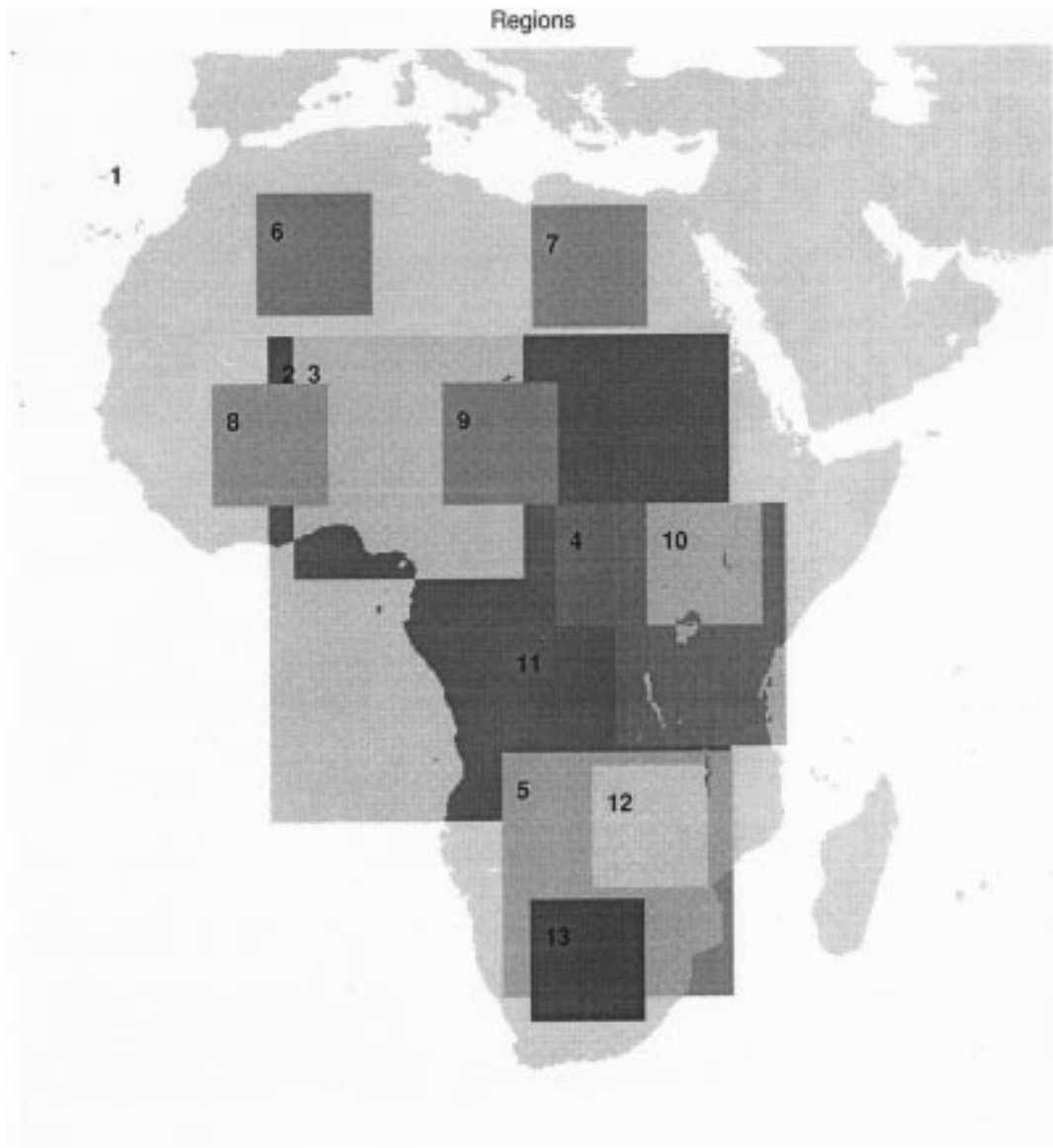


Fig. 1. African regions selected for spatial coherence evaluation.

TABLE II

FUNCTIONAL CHARACTERISTICS OF DETAILED REGIONS IN FIG. 1. ALL REGIONS ARE SQUARE SHAPED AND POWER OF TWO FOR APPLICATION OF A FAST WAVELET TRANSFORM. COVER TYPES: 1 = WOODED GRASSLAND; 2 = BROADLEAF DECIDUOUS FOREST; 3 = BROADLEAF EVERGREEN FOREST; 4 = GRASSLAND; AND 5 = BARE GROUND. CHARACTERIZATION IS TAKEN FROM ANCILLARY SOURCES [26], [27]. LAND COVER IS GIVEN IN DECREASING ORDER OF COVERAGE

Region	Cover type	Wet periods	Region	Cover type	Wet periods
R-2	1, 3, 2	mixed	R-9	1, 2	'summer' greenest
R-3	1, 2	"summer" rains			and few rains
R-4	1, 2, 4	mixed	R-10	1, 4	mixed-dry
R-5	1, 4, 2	Nov - Feb few rains	R-11	3, 2	year-round rains
R-6	5	year-round dry	R-12	2, 4	Nov - Feb few rains
R-7	5	year-round dry	R-13	1, 4	Nov - Feb few rains
R-8	1	"summer" rains			

limited to this case. In fact, the wavelet representation offers different choices for the transform and filters that could be tuned to specific spatial structures (or geometries) of the image for its optimal representation [13], [15], [33], and [34], .

Multiresolution wavelet analysis looks at an image or signal at different spatial scales producing a sequence of approximations of the original at each resolution. Starting with the original image $c_0(x, y)$, successive convolutions with a filter derived from a scaling function produce smoothed data $c_i(x, y)$ at each resolution i . The signal difference between two consecutive resolutions provide the wavelet coefficients $w_i(x, y)$, $= c_{i-1}(x, y) - c_i(x, y)$, and the set of all $w_i(x, y)$ for each resolution i constitutes a wavelet plane. The original image can be reconstructed by addition of all wavelet planes with the last smooth plane, $c_p(x, y)$. This can be expressed as

$$c_0(x, y) = c_p(x, y) + \sum_{i=p}^1 w_i(x, y). \quad (1)$$

harmonic analysis efforts [14], [19], and [30]–[32], the mathematical framework for image smoothness classification is not

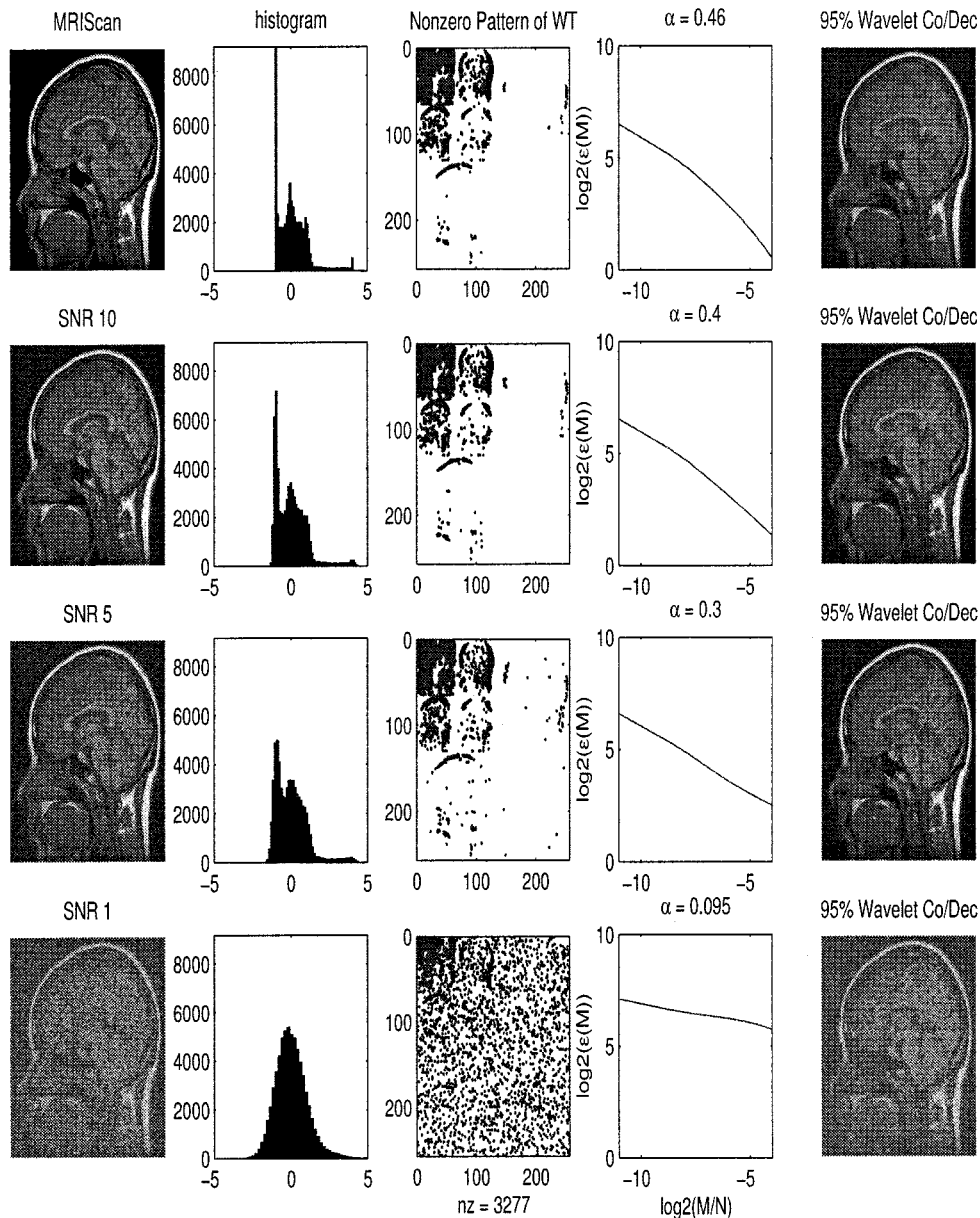


Fig. 2. Column 1: gray-scale MRI brain scan at different SNRs (pixel variance/noise power): 50 (original), 10, 5, and 1); column 2: histograms of normalized MRI gray values; column 3: locations of highest 5% quantized wavelet coefficients; column 4: coherence plots with rate of decay α ; and column 5: reconstruction using highest 5% quantized wavelet coefficients.

Thus, the wavelet approach models the image as the combination of a large selection of different waves that could be tuned for a better approximation of the coherence, and details of the image. This tuning feature makes multiresolution wavelet analysis an attractive framework to study image coherence. It is based on the properties used for image compression and noise removal. If an image is noisy, the wavelet coefficients will have a noise component as well. Coherent components of the signal will be concentrated in a small number of coefficients in the wavelet domain. The noise energy is expected to have negligible wavelet coefficients and could be filtered out. Thus, the construction of wavelets begins by designing the filters that should be optimized to produce a minimum of nonnegligible wavelet coefficients. This depends mostly on the regularity of the image, the number of vanishing moments of the filter and the size of its support [35], [15]. We have used a Coiflet wavelet with four

vanishing moments to characterize the variability in smoothness of the NDVI imagery. In fact, NDVI imagery comprises images having high regularity between few cloud singularities to images with an increasing density of cloud singularities. For the first set of images, a wavelet with many vanishing moments will approximate well its smoothness. For the last, we should further decrease the size of its support at the expense of reducing the number of vanishing moments and increasing the number of nonnegligible wavelet coefficients. We used the public domain software package, Wavelab, for the wavelet analysis, and in particular, to generate Coiflet wavelets [36].

C. Smoothness Spaces

Recently, Devore *et al.* [16], [14], and Donoho and Johnstone [18] have introduced a new way to look at the compression and estimation of natural noisy images. They observed

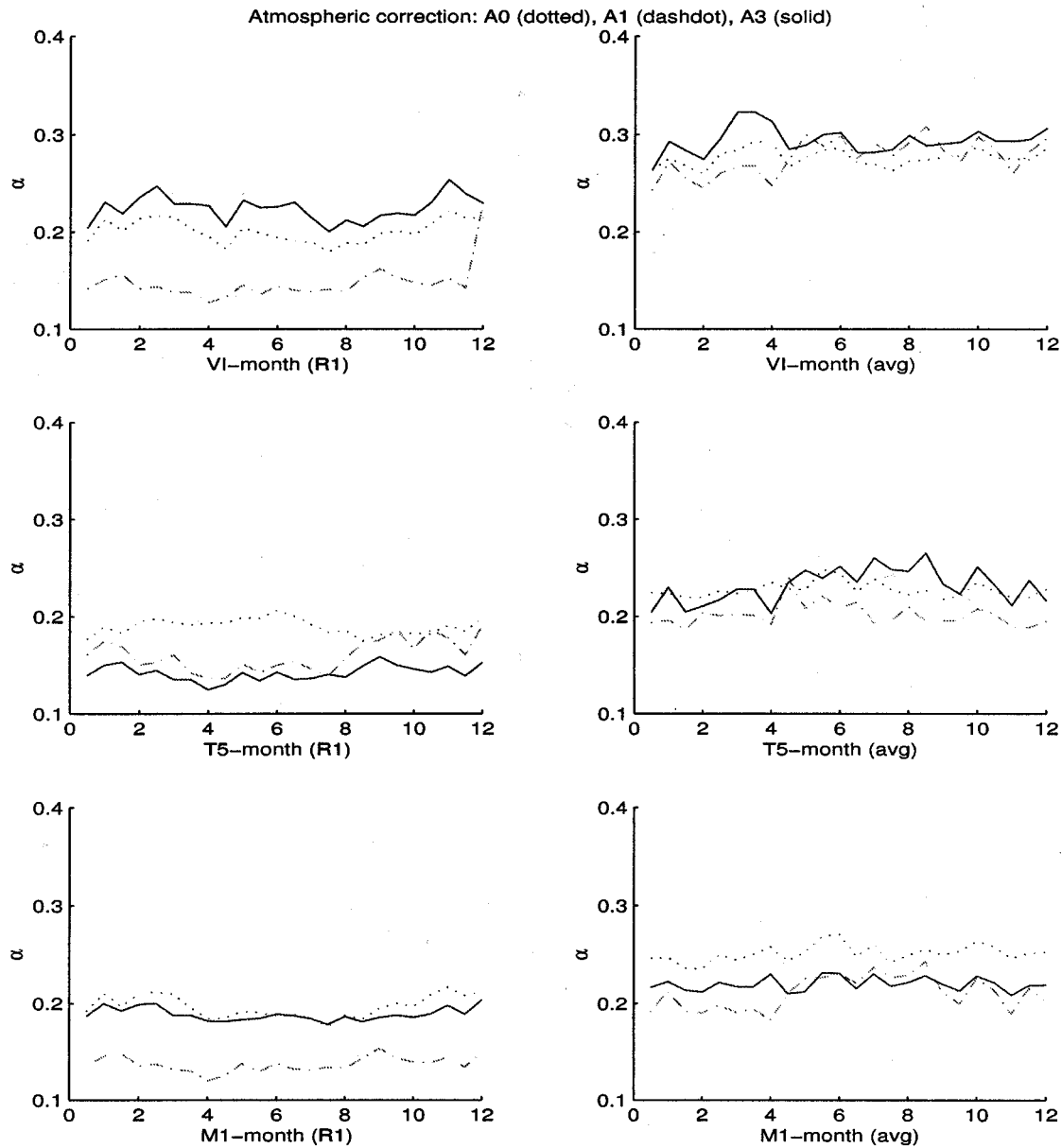


Fig. 3. Global and regional average complexity indexes by month of each compositing with no correction (AO, dotted line), Rayleigh and ozone (A1, dashdot line) and Rayleigh, ozone, and water vapor (A3, solid line) atmospheric correction technique.

that when an image is approximated by its M largest quantized wavelet coefficients, the l^p approximation error $\epsilon(M)$ is proportional to $M^{-\alpha/2}$. They have shown that the rate of decay α characterizes well the smoothness of the image, since it guarantees its membership in the Besov space $\mathcal{B}_q^\alpha(l^q(I))$, where $q = 1/(\alpha/2 + 1/p) = p/(1 + \alpha p/2) < p$. See the Appendix for definitions.

Roughly speaking, functions in $\mathcal{B}_p^\alpha(l^p(I))$ have α “derivatives” in $l^p(I)$. Since $q < p$, the parameter q can measure more subtle gradations in smoothness [16]. Specifically, the improvement resides in the difference between linear and nonlinear wavelet approximation. An image g is approximated by \tilde{g}_M in a linear fashion, selecting its M coarsest level quantized wavelet coefficients. On the other hand, in a nonlinear approximation \tilde{g}_M is given by choosing its M largest quantized wavelet coefficients. In this paper, quantization is given by the nonlinear

approach

$$\tilde{w}_i(x, y) = \begin{cases} w_i(x, y), & M \text{ largest wavelet coefficients} \\ 0, & \text{otherwise.} \end{cases}$$

Bounds for the l^p approximation error in a linear approach are rather sharp

$$\|g - \tilde{g}_M\|_{l^p} \leq CM^{-\alpha/2} \|g\|_{\mathcal{B}_p^\alpha(l^p(I))}$$

i.e., no numbers $\beta < \alpha$ or $q < p$ can be substituted in the norm of g on the right side [16]. On the other hand, bounds for a nonlinear method are more flexible

$$\|g - \tilde{g}_M\|_{l^p} \leq CM^{-\alpha/2} \|g\|_{\mathcal{B}_q^\alpha(l^q(I))},$$

where $q < p$ is defined as before. More images can be approximated to order $M^{-\alpha/2}$ with a nonlinear approach, since it

TABLE III

SEASONAL AVERAGE AND STANDARD DEVIATION OF THE COMPLEXITY INDEX α OF EACH COMPOSITING TECHNIQUE WITH NO CORRECTION (AO), RAYLEIGH AND OZONE (A1), AND RAYLEIGH, OZONE, AND WATER VAPOR (A3) ATMOSPHERIC CORRECTIONS IN REGIONS R3, R4, AND R5. THE HIGHEST α VALUES BY SEASON ARE BOLDED IN EACH ROW. THE SMALLEST α VALUES BY METHOD AND REGION ARE UNDERLINED IN EACH COLUMN. THE MEAN VALUE α AND ITS STD ARE SCALED BY 100

Composite	NDVI			T5			M1		
	Atmospheric Correction			Atmospheric Correction			Atmospheric Correction		
Season	A0	A1	A3	A0	A1	A3	A0	A1	A3
Region 3									
Jan-Mar	33 ± 2	35 ± 2	36 ± 2	28 ± 3	27 ± 2	30 ± 2	30 ± 3	29 ± 3	29 ± 2
Apr-Jun	32 ± 1	33 ± 1	35 ± 2	26 ± 2	22 ± 1	27 ± 2	29 ± 2	27 ± 1	29 ± 2
Jul-Sep	<u>29</u> ± 2	<u>28</u> ± 2	31 ± 3	23 ± 2	<u>17</u> ± 1	<u>22</u> ± 2	<u>25</u> ± 3	<u>23</u> ± 2	<u>25</u> ± 3
Oct-Dec	33 ± 3	35 ± 4	36 ± 3	26 ± 3	25 ± 2	29 ± 3	30 ± 4	28 ± 4	29 ± 3
Region 4									
Jan-Mar	<u>25</u> ± 2	23 ± 3	<u>25</u> ± 3	<u>21</u> ± 2	16 ± 1	18 ± 2	<u>21</u> ± 2	19 ± 3	<u>21</u> ± 2
Apr-Jun	26 ± 2	23 ± 4	27 ± 2	21 ± 2	16 ± 2	18 ± 4	23 ± 3	19 ± 3	22 ± 2
Jul-Sep	27 ± 2	27 ± 2	29 ± 2	22 ± 1	17 ± 1	22 ± 1	25 ± 2	22 ± 1	24 ± 1
Oct-Dec	27 ± 2	<u>22</u> ± 4	29 ± 2	21 ± 1	<u>15</u> ± 1	<u>17</u> ± 2	23 ± 2	<u>18</u> ± 2	22 ± 2
Region 5									
Jan-Mar	26 ± 4	<u>19</u> ± 3	27 ± 5	<u>20</u> ± 4	<u>16</u> ± 2	<u>15</u> ± 2	<u>21</u> ± 4	<u>15</u> ± 2	<u>21</u> ± 4
Apr-Jun	28 ± 1	26 ± 6	30 ± 1	26 ± 2	23 ± 4	22 ± 6	26 ± 1	21 ± 5	23 ± 1
Jul-Sep	26 ± 1	30 ± 2	28 ± 1	24 ± 2	24 ± 2	27 ± 2	24 ± 1	25 ± 2	23 ± 1
Oct-Dec	<u>25</u> ± 3	26 ± 3	26 ± 4	22 ± 2	17 ± 2	23 ± 3	24 ± 3	21 ± 2	22 ± 3

only requires that g have α derivatives in $l^q(I)$ and not in $l^p(I)$. Moreover, if an image has at most β derivatives in $l^q(I)$ and α derivatives in $l^p(I)$, then $\beta > \alpha$ because $q < p$ [16].

In summary, the decay of the error $\epsilon(M)$ is related to $\|g\|_{\mathcal{B}_p}$ by the following theorem.

Theorem 1: The nonlinear approximation error $\epsilon(M) = \|g - \tilde{g}_M\|_{l^p}$ is $O(M^{-\alpha/2})$, if and only if, g belongs to $\mathcal{B}_q^\alpha(l^q(I))$.

Devore *et al.* [16] and Mallat [15] provide a complete proof of the theorem and add other important material for applications in image compression. In practice, in a log-log graph of the L^p approximation error versus largest nonzero coefficients, the data should lie on a straight line with slope $-\alpha/2$. The rate of decay α will be computed from a linear least square fit. In this sense, we say that the image smoothness is at most α .

D. An Example

As an illustration of the complexity index, we took an original MRI and added Gaussian noise at three different SNR levels (SNR = 10, SNR = 5, and SNR = 1). SNR is computed as the ratio between image variance and noise power. The MRI (with an original SNR = 50) was included in the Wavelab package [36] and originally obtained from the National Institute of Health (NIH) image program, a public domain software package distributed freely by the NIH.

Coiflet wavelet decomposition was computed on each of the images and the rate of decay α were derived from a least square fit of the L^2 approximation error versus largest nonzero coefficients. Fig. 2 presents the results of the coherence complexity

curves corresponding to each of the MRI noisy images. We show the histograms of each normalized MRI gray value before the wavelet decomposition. Although the original structure of the image is gradually degraded until a Gaussian shape distribution is obtained, the main low frequency components maintain a recognizable MRI structure. The location of 5% highest quantized wavelet coefficients in a multiresolution plane are shown in column 3. Basically, the low frequency content (smoothest part) of the image is the main contributor to this 5% approximation. The main effect of adding noise into the image is the noticeable spread of this 5% in the wavelet multiresolution plane. In particular, the increasing contribution of high frequency components makes the image less coherent. The graphs of the approximation error (column 4), from which the complexity index α is derived, summarize the previous observations. The rate of decay α decreases with SNR from 0.46 to 0.09. The curve of the approximation error becomes flatter as SNR decreases, resulting in difficulties to reconstruct the details of noisy images. In fact, column 5 shows the reconstruction obtained from the 5% approximation. This result shows the potential to characterize an image compression or noise reduction algorithm in terms of Besov spaces theory as Devore *et al.* [16], [14] and Donoho and Johnstone [18] suggested.

III. RESULTS

Applying the complexity index to compare the spatial coherence of NDVI images derived from the aforementioned com-

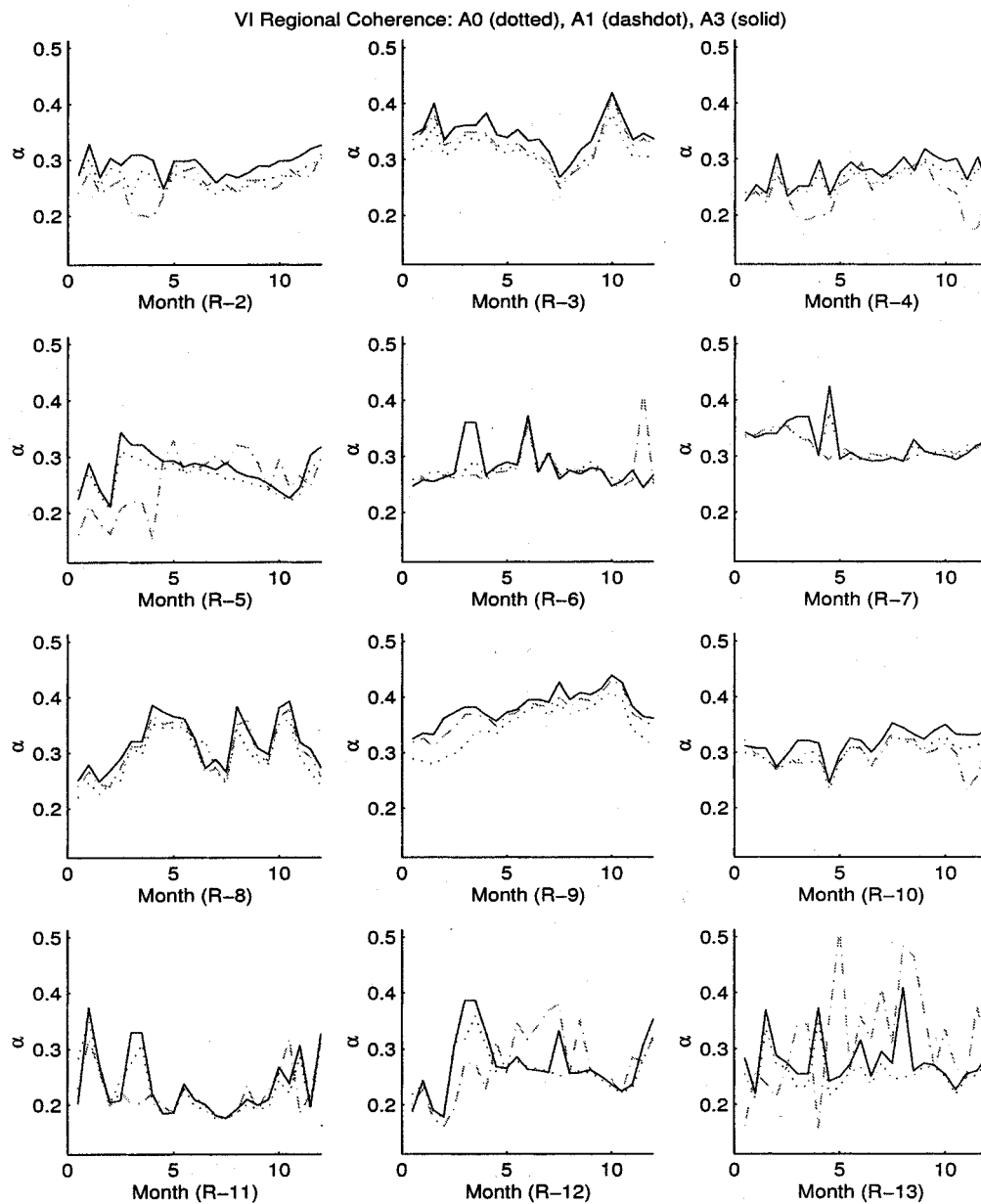


Fig. 4. Regional complexity indexes for maximum NDVI 15 day compositing with no correction (A0, dotted line), Rayleigh and ozone (A1, dash-dot line) and Rayleigh, ozone and water vapor (A3, solid line) atmospheric correction technique.

posite and atmospheric correction techniques, we found that α ranges from 0.1 to 0.5. This variation could be linked to climatic and phenologic regional and seasonal characteristics as follows.

Fig. 3 shows the temporal variation of two global complexity indexes. The first one is derived from direct computation of α , when region R1 (continental Africa) is used as input image. The second α is the average of the complexity indexes for subregions R2 to R13. As indicated in the previous section, high α values identify images with higher spatial coherence. In this case, as Fig. 3 shows, the maximum NDVI composite technique (VI) with full atmospheric correction (A3) is the method that consistently provides the highest spatial coherence, even at individual regional levels (results not shown). This is consistent with the findings of Holben *et al.* [4], who showed that the maximum NDVI composite technique (VI) efficiently reduces atmospheric effects and cloud contamination making the technique appropriate for vegetation

studies. It also shows that the α averaged from subregions R2 to R13 is higher than the direct α from region R1. This is so since the contribution of the ocean signal, mostly noisy, is higher in region R1 than in the subregions. Standard NDVI images are not usually tuned to give a reliable ocean characterization. In fact, for vegetation studies, the ocean signal is generally filtered out [21]. These results led us to conclude that the values of α averaged from regions R2 to R13 are more likely to characterize the spatial coherence of the global image, since they reduced water noise contributions. Moreover, the discrepancy shown between the α s for the maximum NDVI composite (VI) with partial and full atmospheric correction (A1 and A3, respectively) is also explained by noise contributions from the ocean.

None of the temporal complexity index plots in Fig. 3 show a clear seasonal dependency. This could be explained by the complex phenologic mixture of land cover acting at this continental

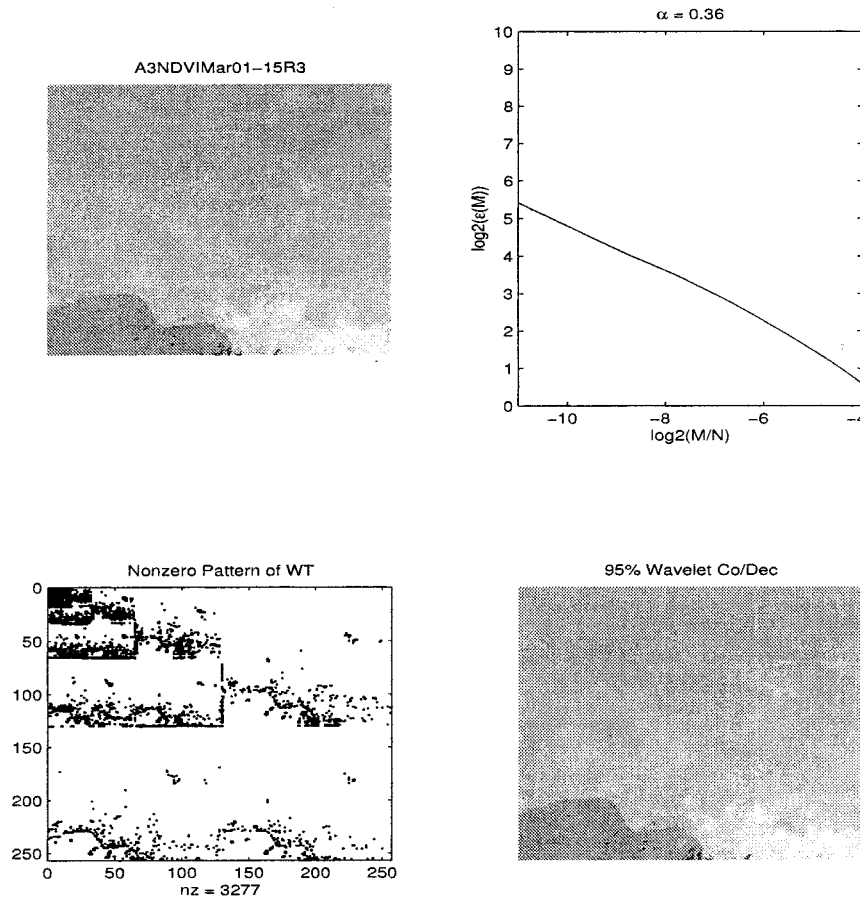


Fig. 5. Complexity index for a gray-scale NDVI-AVHRR image in a dry season.

scale. In order to study seasonal sensitivity, we have summarized in Table III the temporal variability of α for regions R3, R4, and R5. According to Table II, these regions have different seasonal and phenologic characteristics. Region R3, which includes the Sahel, regularly shows monsoon summer rainfall seasonality. R4 is a mixture of wooded and grassland, mostly dry, with no clear wet seasonality. R5 on the other hand, includes a deciduous forest land cover with few rains during November–February. In all these cases, region R3 shows higher α values than R4 and R5. This should be so, since the Sahel presents a rich vegetation signal and the NDVI has been shown to well characterize this land cover [37], [38]. Table III makes clear the negative correlation between the complexity index and wet seasonal periods. In region R3, the “summer” rainfall seasonality is very well identified by the lowest complexity index (values underlined). In the other regions, the lowest α values go well with the expected dry season periods of November to February.

Table III also shows clearly that VI compositing with full A3 atmospheric correction is the method with highest spatial coherence in all regions and most of the seasons (values **bolded**, column NDVI-A3). Only during the period from July to September does NDVI compositing with partial A1 atmospheric correction present an anomalous highest α value of 0.30 for region R5. During the same period and in the same region, NDVI with full A3 atmospheric correction has the second highest α value of 0.28. To find out potential causes for this anomalous case and to characterize regions by its

spatial coherence, Fig. 4 presents the temporal variability of the complexity index for the NDVI compositing with A0, A1, and A3 atmospheric correction methods in all 12 subregions (R2–R13). Region R2 presents nonseasonal patterns and is similar to region R1. It has a complex land cover mixture. However, R2 will have higher α values than R1 due to a lower noise contamination from the ocean. As explained earlier, regions R3 and R8, which are subregions of the Sahel, present the natural drop in α during the “summer” rainfall season. Although region R9 has similar phenologic and climatic characteristics as region R8, interestingly, it shows high α values. There is not a clear explanation other than the change of rainfall gradient (see Table II). The characteristics of the complexity index for R4 seems to be explained by the mixture of its two dominant classes (a dry and wet wooded grassland) that are very well represented by region R10. An erratic behavior in the complexity index at the beginning of the year is found in region R5. This is mainly due to the similar behavior shown by its dominant landcover (region R12). Among all regions, R5, R12, and R13 possess the most unstable characterization by the complexity index. This is perhaps because of the mixture of grassland and savanna during the dry season. In fact, Nicholson *et al.* [26] found that the southern Africa savanna has a longer rainy season than the Sahelian region but with comparable annual rainfall amounts. Their study found that while rainfall reaches approximately 170 to 190 mm in three months in region R12, it barely reaches 100 mm per month in region

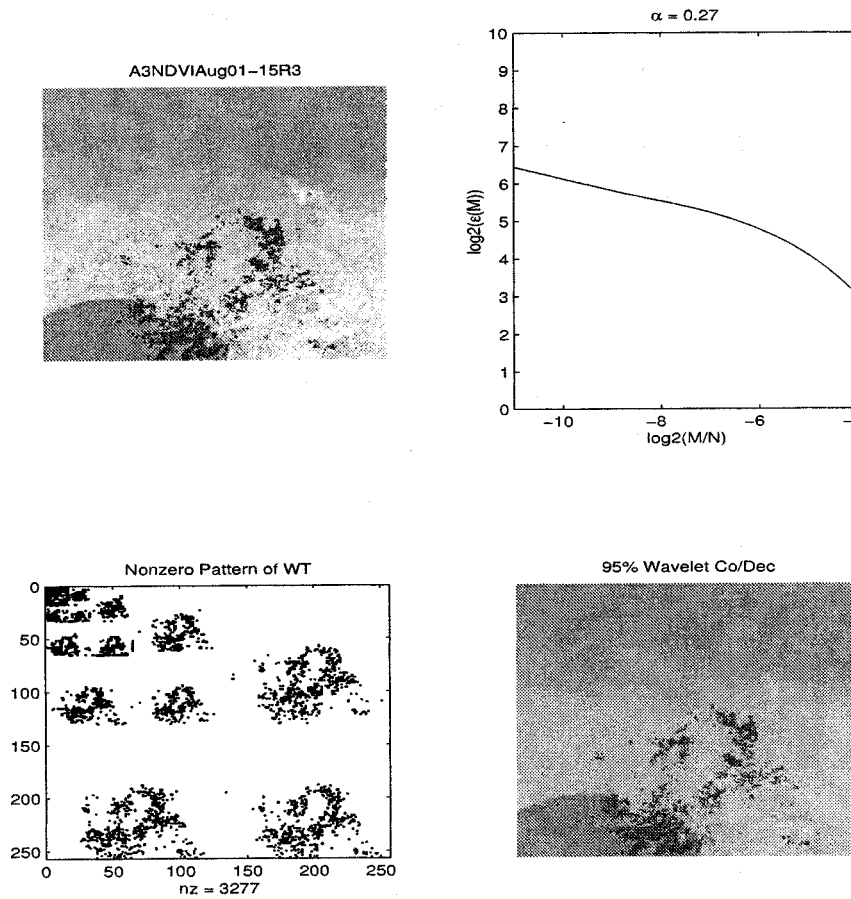


Fig. 6. Complexity index for a gray-scale NDVI-AVHRR image in a rainy season.

R13. In both regions, however, rainfall continues intermittently throughout the dry season. This contrast could be explained by the nature of the rain-bearing systems affecting southern Africa [26]. This is manifested in the high variance of the complexity index for region R5 (see Table III). The desert regions, R6 and R7, show stable α values with nonseasonal pattern. Region R11, part of the equatorial forest with year round rains, has consistently one of the lowest α values between the regions. Specifically, during May and October, the complexity index falls to its lowest values. During this period, the likelihood of cloud-free images for that region is low.

Figs. 5 and 6 show the differences in spatial coherence between images during dry season and when cloud contamination is reduced. Although the maximum NDVI composite reduces the cloud contamination [4], the spatial coherence is lower when we have fewer useful days in the composite. These figures support the results outlined in Section II: an image with less spatial coherence will require more wavelet coefficients than a smoother image to get a comparable approximation. Using the highest 5% of the wavelet coefficients, we have better approximation for the NDVI image taken from a dry season (Fig. 5) than the one taken from the rainy season (Fig. 6).

IV. DISCUSSION AND CONCLUSIONS

We examined the role of harmonic analysis in characterizing the spatial coherence of an image in terms of smoothness membership in Besov spaces. The estimates of the complexity

index are consistent with visual evaluation and with the physics of the image collection process. We have also established the framework of Besov space for characterizing quantitatively the quality of various compositing and atmospheric correction techniques. In particular, we showed that the maximum NDVI with Rayleigh, ozone, water vapor correction provides the highest spatial coherence among the other techniques explored. The complexity index ranges from 0.1 to 0.5 and agrees well with phenologic characterizations of regional land cover. The complexity index is regionally dependent and is higher for images taken from dry periods than from wet periods, where residual cloudiness interference is more likely to appear.

Our results allow the development of quality characterizations for remotely sensed data. The complexity index assesses the overall quality of the image. It also provides a diagnosis of potential local problems such as contamination by clouds.

APPENDIX HILBERT SPACE

We briefly review the following elementary mathematical concepts of linear operators and Hilbert spaces necessary to introduce Besov spaces.

- The **norm** of a nonzero vector g in a vector space H is positive and satisfies:

- 1) triangle inequality: $\|f + g\| \leq \|f\| + \|g\|$;
- 2) scaling property: $\|\alpha g\| = |\alpha| \|g\|$.

There are many possible choices of such norm. We focus on the use of l^p norms with $0 < p < \infty$ as error metrics. These norms are defined by

$$\|f - g\|_{l^p} \doteq \left(\sum_{n=-\infty}^{n=\infty} |f(n) - g(n)|^p \right)^{1/p}.$$

When $p = 2$, we have mean squared error (MSE) metric.

- A sequence $\{g_n\}_{n \in \mathcal{N}}$ is a Cauchy sequence if for any $\epsilon > 0$, there is an l such that $\forall n, m > l, \|g_n - g_m\| < \epsilon$.
- A vector space H is **complete** if every Cauchy sequence in H converges to an element of H .
- A **Banach space** is a vector space H , which has a norm and is complete.
- A Hilbert space H is a Banach space with a norm that can be expressed as an inner product. In this case, the **inner product** of two vectors $\langle f, g \rangle$ in H satisfies

- 1) Linearity with respect to its first argument

$$\forall \lambda_1, \lambda_2 \in \mathbb{C}, \quad \langle \lambda_1 f_1 + \lambda_2 f_2, g \rangle = \lambda_1 \langle f_1, g \rangle + \lambda_2 \langle f_2, g \rangle.$$

- 2) Hermitian symmetry $\langle f, g \rangle = \langle g, f \rangle^*$, where $*$ means complex conjugate.

- 3) Positiveness: $\langle x, x \rangle \geq 0$ and $\langle x, x \rangle = 0$ if and only if $x = 0$.

For example, the inner product between two vectors can be defined by

$$\langle f, g \rangle = \sum_{n=-\infty}^{n=\infty} f(n)g^*(n)$$

and it corresponds to an $l^2(Z)$ norm: $\|g\|^2 = \langle g, g \rangle = \sum_{n=-\infty}^{n=\infty} |g(n)|^2$.

- The Besov space $B_q^\alpha(L^p(I))$ is the collection of functions g with finite L^p norm ($g \in L^p(I)$) that are defined on the unit square $I = [0, 1]^2$ and have a common α "smoothness" for $0 < p < \infty$ and $q = 1/(\alpha/2 + 1/p)$. The smoothness of the Besov space is reflected in its norm $\|g\|_{B_q^\alpha(L^p(I))} < \infty$. The norm measures α "derivatives" of the function and it is given by

$$\|g\|_{B_q^\alpha(L^p(I))} = \|g\|_{(L^p(I))} + \left(\int_0^\infty \left[\frac{t^{-\alpha}}{t} \omega(g, t)_p \right]^q \right)^{1/q}$$

where $\omega(g, t)_p = \sup_{|h| \leq t} (\int_{I_h} |g(x+h) - g(x)|^p dx)^{1/p}$, and $I_h = \{x \in I | x+h \in I\}$ [16].

ACKNOWLEDGMENT

The authors would like to thank S. Los, J. Kendall, and L. Giglio for assistance. The authors also thank two anonymous reviewers for their comments. They would also like to thank members of the Global Inventory Mapping and Monitoring Study (GIMMS) Group, NASA/Goddard Space Flight Center, Greenbelt, MD, for their assistance in the processing of the remote sensing data sets presented in this paper.

REFERENCES

- [1] C. J. Tucker, "Red and photographic infrared linear combinations monitoring vegetation," *Remote Sens. Environ.*, vol. 8, pp. 127–150, 1979.
- [2] P. J. Sellers, "Canopy reflectance, photosynthesis and transpiration," *Int. J. Remote Sensing*, vol. 6, pp. 1335–1372, 1985.
- [3] C. J. Tucker and P. J. Sellers, "Satellite remote sensing of primary production," *Int. J. Remote Sensing*, vol. 7, pp. 1395–1416, 1986.
- [4] B. N. Holben, "Characteristics of maximum-value composite images from temporal AVHRR data," *Int. J. Remote Sensing*, vol. 7, no. 11, pp. 1417–1434, 1986.
- [5] D. Tanrè, B. N. Holben, and Y. J. Kaufman, "Atmospheric correction algorithm for NOAA-AVHRR products: Theory and application," *IEEE Trans. Geosci. Remote Sensing*, vol. 30, pp. 231–248, Jan. 1992.
- [6] E. F. Vermote, D. Tanrè, J. L. Deuze, M. Herman, and J. J. Morcrette, "Second simulation of the satellite signal in the solar spectrum: An overview," *IEEE Trans. Geosci. Remote Sensing*, vol. 35, pp. 675–686, May 1997.
- [7] N. Z. El Saleous, E. F. Vermote, C. O. Justice, J. R. G. Townshend, C. J. Tucker, and S. N. Goward, "Improvements in the global biospheric record from the advanced very high resolution radiometer (AVHRR)," *Int. J. Remote Sensing*, vol. 21, no. 6, pp. 1251–1277, 2000.
- [8] C. E. Woodcock, A. H. Strahler, and D. L. B. Jupp, "The use of variograms in remote sensing: I. Scene models and simulated images," *Remote Sens. Environ.*, vol. 25, pp. 323–348, 1988.
- [9] —, "The use of variograms in remote sensing: II. Real digital images," *Remote Sens. Environ.*, vol. 25, pp. 349–379, 1988.
- [10] D. L. B. Jupp, A. H. Strahler, and C. E. Woodcock, "Autocorrelation and regularization in digital images: I. Basic theory," *IEEE Trans. Geosci. Remote Sensing*, vol. 26, pp. 463–473, July 1988.
- [11] J. Cihlar, D. Manak, and M. D'Iorio, "Evaluation of compositing algorithms for AVHRR data over land," *IEEE Trans. Geosci. Remote Sensing*, vol. 32, pp. 427–437, Mar. 1994.
- [12] M. Wright and A. Chorin. (1999, Apr.). Tech. Rep., Mathematics and Science, Div. Math. Sci., Nat. Sci. Foundation, [Online] Available: <http://www.nsf.gov/mps/dms/start.htm>
- [13] S. G. Mallat, "A theory for multiresolution signal decomposition: The wavelet representation," *IEEE Trans. Pattern Anal. Machine Intell.*, vol. 11, pp. 674–693, July 1989.
- [14] R. A. DeVore and B. J. Lucier, "Classifying the smoothness of images: Theory and applications to wavelet image processing," in *Proc. 1st Int. Conf. Image Processing (ICIP-94)* Austin, TX, Nov. 1996.
- [15] S. G. Mallat, *A Wavelet Tour of Signal Processing*. San Diego, CA: Academic, 1998.
- [16] R. A. DeVore, B. Jawerth, and B. J. Lucier, "Image compression through wavelet transform coding," *IEEE Trans. Inform. Theory*, vol. 38, pp. 719–746, Mar. 1992.
- [17] R. A. DeVore and B. J. Lucier, "Fast wavelet techniques for near image processing," in *Proc. 1st Int. Conf. Image Processing (ICIP-94)* Austin, TX, Nov. 1996.
- [18] D. L. Donoho and I. M. Johnstone, "Ideal spatial adaptation via wavelet shrinkage," *Biometrika*, vol. 81, pp. 425–455, December 1994.
- [19] D. L. Donoho, M. Vetterli, R. A. DeVore, and I. Daubechies, "Data compression and harmonic analysis," *IEEE Trans. Inform. Theory*, vol. 44, pp. 2435–2476, Oct. 1998.
- [20] R. A. DeVore, W. Shao, J. F. Pierce, E. Kaymaz, B. T. Lerner, and W. J. Campbell, "Using nonlinear wavelet compression to enhance image registration," *Proc. SPIE*, vol. 3078, pp. 539–551, Apr. 1997.
- [21] C. J. Tucker, R. Mahoney, N. Z. El Saleous, S. Los, E. Vermote, M. Paris, M. Brown, D. Grant, and A. Morahan, "The global inventory mapping and monitoring study 1981–1999 AVHRR 8-km data set," *Int. J. Remote Sensing*, to be published.
- [22] M. E. James and S. N. Kalluri, "The pathfinder AVHRR land data set: An improved coarse-resolution data set for terrestrial monitoring", to be published.
- [23] S. Los, C. O. Justice, and C. J. Tucker, "A global 1° by 1° NDVI data set for climate studies derived from GIMMS continental NDVI data," *Int. J. Remote Sensing*, vol. 15, pp. 3493–3518, Nov. 20, 1994.
- [24] J. P. Malingreau and A. S. Belward, "Recent activities in the European community for the creation of global AVHRR data sets," *Int. J. Remote Sensing*, vol. 15, pp. 3397–3416, Nov. 20, 1994.
- [25] E. F. Vermote, N. El Saleous, and B. Holben, "Aerosol retrieval and atmospheric correction," in *Advances in the Use of NOAA AVHRR Visible and Near Infrared Channels Using Ocean and Cloud Views*, G. D'Souza, A. S. Belward, and J.-P. Malingreau, Eds. Dordrecht, The Netherlands: Kluwer, 1996.
- [26] S. E. Nicholson, J. Kim, M. B. Ba, and A. R. Lare, "The mean surface water balance over Africa and its interannual variability," *J. Climate*, vol. 10, pp. 2981–3002, Dec. 1997.

- [27] M. C. Hansen, R. S. Defries, J. R. G. Townshend, and R. Sohlberg, "Global land cover classification at 1km spatial resolution using a classification tree approach," *Int. J. Remote Sensing*, vol. 21, no. 6 & 7, pp. 1331–1364, 2000.
- [28] R. S. Defries and J. R. G. Townshend, "NDVI-derived land cover classifications at a global scale," *Int. J. Remote Sensing*, vol. 15, no. 17, pp. 3567–3586, 1994.
- [29] C. J. Tucker and W. W. Newcomb, "AVHRR data sets for determination of desert spatial extent," *Int. J. Remote Sensing*, vol. 15, no. 17, pp. 3547–3565, 1994.
- [30] D. L. Donoho, "Unconditional bases are optimal bases for data compression and for statistical estimation," *J. Appl. Comput. Harmon. Anal.*, vol. 1, pp. 100–115, 1993.
- [31] J. L. Starck, F. Murtagh, and A. Bijaoui, *Image Processing and Data Analysis*. Cambridge, U.K.: Cambridge Univ. Press, 1998.
- [32] J. Nuñez, X. Otazu, O. Fors, A. Prades, V. Palá, and R. Arbiol, "Multiresolution-based image fusion with additive wavelet decomposition," *IEEE Trans. Geosci. Remote Sensing*, vol. 37, pp. 1204–1211, May 1999.
- [33] R. R. Coifman and M. V. Wickerhauser, "Entropy based algorithm for best basis selection," *IEEE Trans. Inform. Theory*, vol. 38, pp. 713–746, Feb. 1992.
- [34] J. D. Villaseñor, B. Belzer, and J. Liao, "Image coding using wavelet transform," *IEEE Transactions on Image Processing*, vol. 4, pp. 1053–1060, August 1995.
- [35] I. Daubechies, *Ten Lectures on Wavelets*. Philadelphia, PA: SIAM, 1992.
- [36] J. Buckheit, S. Chen, D. Donoho, and I. Johnstone. (1995) Wavelab Matlab software .701. [Online]. Available: <http://palyfair.stanford.edu/wavelab/>.
- [37] S. E. Nicholson, C. J. Tucker, and M. B. Ba, "Desertification, drought, and surface vegetation: An example from the West African Sahel," *Bull. Amer. Meteorol. Soc.*, vol. 79, pp. 815–829, May 1998.
- [38] C. J. Tucker and S. E. Nicholson, "Variations in the size of the Sahara desert from 1980 to 1997," *Ambio*, vol. 28, pp. 587–591, Nov. 1999.

Jorge E. Pinzón received the B.Sc. degree in mathematics and the B.Sc. degree in computer science from the Universidad de los Andes, Bogotá, Colombia, in 1985 and 1986, respectively, and the M.S. and Ph.D. degrees in applied mathematics from the University of California, Davis, in 1996 and 1998, respectively.

He was a Postdoctoral Fellow with the University of Maryland, College Park, for two years, and is currently working with Science Systems and Applications, Inc. (SSAI), Biospheric Sciences Branch, NASA/Goddard Space Flight Center, Greenbelt, MD, as a Senior Scientist. His research interests include data representation and pattern recognition in time series and remote sensing.

Dr. Pinzón is a member of SIAM, IEEE Geoscience and Remote Sensing Society, AAAS, and AMS.

John F. Pierce received the Ph.D. degree in mathematics from the University of California, Santa Cruz, in 1981, and the Ph.D. degree in physics from University of Houston, Houston, TX, in 1992.

He is currently with the Department of Mathematics, U.S. Naval Academy, Annapolis, MD. His current research interests are in signal representation and feature extraction from multi- and hyperspectral data, computer image analysis, and optical character recognition using multiresolutional tools, statistical learning machines, and neural nets. He also focuses on questions of nonlinear stability and bifurcation in continuum mechanics.

Compton J. Tucker received the B.S. degree in biology, the M.S. degree, and the Ph.D. degree in forestry, all from Colorado State University, Fort Collins, in 1969, 1973, and 1975, respectively.

He has been at NASA/Goddard Space Flight Center, Greenbelt, MD, since 1975. His research activities involve the use of satellite data to study tropical deforestation, desertification, ecologically-coupled diseases, and terrestrial primary production.

Molly E. Brown received the B.S. degree in biology and environmental sciences from Tufts University, Medford, MA, in 1991, and the M.A. in geography from the University of Maryland, College Park, in 1998, where she is currently pursuing the Ph.D. degree.

She is currently in the Biospheric Sciences Branch, NASA/Goddard Space Flight Center, Greenbelt, MD. She spent three years in West Africa in the U.S. Peace Corps. Her current research interests include vegetation monitoring in semi-arid regions, interdisciplinary research that joins socio-economic and remotely sensed data, and improving systems that use vegetation indices to give early warning of food insecurity and disease outbreak in developing regions.